Cytometry PART A
ISAC
Journal of Quantitative Cell Science

MIFlowCyt

Kinetics of *Mimivirus* Infection Stages Quantified Using Image Flow Cytometry

Liran Ben Yaakov,[1*] Yael Mutsafi,[2] Ziv Porat,[3] Tali Dadosh,[4] Abraham Minsky[1*]

[1]Department of Structural Biology, Weizmann Institute of Science, 7610001, Rehovot, Israel

[2]Biochemistry and Biophysics Center, NHLBI, NIH, 50 South Drive, 20892, Bethesda, Maryland, USA

[3]Life Sciences Core Facilities, Weizmann Institute of Science, Rehovot, 7610001, Israel

[4]Chemical Research Support, Weizmann Institute of Science, Rehovot, 7610001, Israel

Received 26 January 2019; Revised 19 March 2019; Accepted 1 April 2019

Grant sponsor: Israel Science Foundation (ISF), Grant number 813/14; Grant sponsor: Minerva Stiftung, Grant number 910217

Additional Supporting Information may be found in the online version of this article.

*Correspondence to: Liran Ben Yaakov, Department of Structural Biology, Weizmann Institute of Science, Rehovot, 76100, Israel. Email: liran.ben-yaakov@weizmann.ac.il; or Abraham Minsky, Department of Structural Biology, Weizmann Institute of Science, Rehovot, 7610001, Israel. Email: avi.minsky@weizmann.ac.il

Published online 24 April 2019 in Wiley Online Library (wileyonlinelibrary.com)

DOI: 10.1002/cyto.a.23770

Abstract

Due to the heterogeneity of viruses and their hosts, a comprehensive view of viral infection is best achieved by analyzing large populations of infected cells. However, information regarding variation in infected cell populations is lost in bulk measurements. Motivated by an interest in the temporal progression of events in virally infected cells, we used image flow cytometry (IFC) to monitor changes in *Acanthamoeba polyphaga* cells infected with *Mimivirus*. This first use of IFC to study viral infection required the development of methods to preserve morphological features of adherent amoeba cells prior to detachment and analysis in suspension. It also required the identification of IFC parameters that best report on key events in the *Mimivirus* infection cycle. The optimized IFC protocol enabled the simultaneous monitoring of diverse processes including generation of viral factories, transport, and fusion of replication centers within the cell, accumulation of viral progeny, and changes in cell morphology for tens of thousands of cells. After obtaining the time windows for these processes, we used IFC to evaluate the effects of perturbations such as oxidative stress and cytoskeletal disruptors on viral infection. Accurate dose-response curves could be generated, and we found that mild oxidative stress delayed multiple stages of virus production, but eventually infection processes occurred with approximately the same amplitudes. We also found that functional actin cytoskeleton is required for fusion of viral replication centers and later for the production of viral progeny. Through this report, we demonstrate that IFC offers a quantitative, high-throughput, and highly robust approach to study viral infection cycles and virus–host interactions. © 2019 The Authors. *Cytometry Part A* published by Wiley Periodicals, Inc. on behalf of International Society for Advancement of Cytometry.

Key terms

Mimivirus; giant viruses; viral factories; image flow cytometry; cytoskeleton; viral–host interactions

THE *Acanthamoeba polyphaga Mimivirus* is a member of the nucleocytoplasmic large DNA viruses (NCLDVs) clade. A notable and characteristic feature of the NCLDVs is the generation of large and elaborate viral factories (VFs) (1–4). *Mimivirus* forms VFs within the host cytoplasm, where viral replication and assembly occur. *Mimivirus* has a complex dsDNA genome, 1.2 Mbp in length, encoding more than 1,000 proteins. Many of these proteins, including translation initiation factors, aminoacyl transfer RNA synthetases, and DNA repair enzymes, are associated with cellular life and were not previously detected in viruses (5,6). Unlike smaller viruses, whose replication relies almost entirely on host-cell factors, *Mimivirus* uses hundreds of its own genes to orchestrate host cell takeover and virion production (6,7). Although the complexity of *Mimivirus* approaches that of bacteria and small eukaryotic cells, *Mimivirus* is nevertheless an obligate parasite. The aspects of cell physiology that are required for *Mimivirus* infection and the virus–host interactions that are critical at various infection stages remain to be defined.

The *Mimivirus* infection cycle takes about 14 h, starting with phagocytosis of the virion by the amoeba (8–10) and escape of the virion contents from the

phagosome into the cytosol. The viral genome is released into the cytosol through a specially modified vertex in the *Mimivirus* icosahedral capsid, termed the "stargate" (8). Shortly thereafter, several replication centers form in the cytoplasm of the infected cell, each originating from an individual *Mimivirus* virion (4). These replication centers eventually coalesce into a single large VF. The *Mimivirus* VF is an elaborate and highly ordered "organelle" (4,8) that consists of large amounts of DNA, hundreds of different virally encoded proteins (7), as well as membranes and capsids at its periphery (11). Within the VF platform, viral replication, transcription, and assembly take place in a highly coordinated manner. Finally, the host cell erupts, and hundreds of virus progeny, large particles about 750 nm in diameter, are released (8,12).

Much of our current knowledge on *Mimivirus* and its infection cycle have been derived from two research directions: bioinformatics and structural studies. The bioinformatics research has provided information on *Mimivirus* gene content, offered putative functional annotations, and explored gene expression throughout the infection cycle (5–7,13). In addition, bioinformatics analyses yielded a phylogenetic overview of the relationship among the known members of the giant viruses and their relationship to the tree of life (5,13–16). Structural methods, such as scanning and transmission electron microscopy, X-ray, AFM (atomic force microscopy), and fluorescence microscopy, have in turn provided insights into the *Mimivirus* virion structure and the viral infection cycle (8,10,17–21).

Here we aimed to complement the existing methodologies by developing a high-throughput method to quantify the progression of *Mimivirus* infection and obtain accurate time windows for various steps in the viral replication cycle. Toward this aim, we used an image flow cytometry (IFC) platform to collect data on large populations of *Mimivirus*-infected cells. Recent works have used IFC to study infection by the intracellular pathogens *Leishmania amazonensis*, *Toxoplasma gondii*, *Blastocystis*, *Mycobacterium tuberculosis*, and *Plasmodium falciparum* (22–26). The current study is the first, to the best of our knowledge, to monitor a viral pathogen by IFC and to follow the kinetics of various intracellular processes associated with viral takeover of the cell. In this study, we demonstrate that IFC can be used to examine temporal and amplitude variation across infected cell populations for key events in cell reprogramming and viral production. IFC can be also used to obtain population responds to factors that perturb viral infection kinetics. We focused specifically on the role of host–cell cytoskeleton in *Mimivirus* infection, but the methods described herein are applicable to many other viral or cellular factors that potentially impact the progression of *Mimivirus* infection.

Materials and Methods

Production of *Mimivirus*

Acanthamoeba polyphaga cells were grown in peptone yeast glucose (PYG) medium including ampicillin (100 μg/ml) and kanamycin (50 μg/ml) at 30°C to near confluence and infected with *Mimivirus* at a multiplicity of infection (MOI) ~5 as previously described (8). After about 14 h, lysed cell fragments were removed by centrifugation at 100*g* for 20 min at 4°C. The supernatant was centrifuged at 10,000*g* for 30 min at 4°C to pellet viruses. The pellet was resuspended in 10 ml phosphate buffered saline (PBS) and centrifuged again at 10,000*g* for 30 min at 4°C. The resulting pellet was resuspended in 10 ml PBS including ampicillin (100 μg/ml) and kanamycin (50 μg/ml) and passed through a 1.2 μm filter.

Sample Preparation for IFC Imaging

A. polyphaga cells were infected with *Mimivirus* at MOI ~ 5. Infection was synchronized by washing away virions with PYG medium 30 min after infection. At the indicated times postinfection (PI), the infected cells were washed with cold PBS. The flasks were then shaken vigorously for a few seconds to detach the cells, which were then transferred rapidly into 50 ml tubes containing the fixation agents 4% formaldehyde and 0.5% glutaraldehyde (EMS), in PBS for 15 min at room temperature (RT). This procedure helped to preserve cell morphology. The fixed cells were collected by centrifugation at 700*g* for 10 min at 4°C, and the pellets were transferred into 1.5 ml tubes. The samples were washed three times with PBS and permeabilized using 0.1% Triton X-100 (Sigma, St. Louis, MO) for 10 min at RT, washed again three times with PBS, and stained with DAPI (5 μg/ml) diluted 1:1,000, for 1 h at RT. This concentration of DAPI was optimized for visualization of both the cell nucleus and the VF. Finally, the samples were washed with PBS and subjected to flow cytometry. When treatments were applied to cells, they were added immediately after washing away *Mimivirus* at 30 min PI. These treatments consisted of H_2O_2 (500 μM), nocodazole (33 μM), or latrunculin-B (5 μg/ml).

IFC Data Collection

Samples, each containing 3×10^4 cells, were imaged using multispectral imaging flow cytometry (ImageStreamX mark II; Amnis Corp, part of EMD Millipore, Seattle, WA). In most of the experiments, 5,000–30,000 events were acquired per sample. Imaging was performed using 60×/NA = 0.9 lens; the lasers used were: 405 nm (50 mW) for DAPI, and 785 nm (5 mW) for side scatter (SSC) channel imaging. Data were analyzed using image analysis software (IDEAS 6.2; Amnis Corporation, Seattle, WA). Images were compensated for fluorescent dye overlap by using single-stain controls. Data were recorded only for single cells using the "area" and "aspect ratio" (the cell minor axis divided by the cell major axis of the best-fit ellipse) features of the bright field image, and among these, cells in focus were selected using the "gradient RMS" feature (27).

Image Analysis of IFC Data

Feature identification was done in an unbiased manner, using the "find the best feature" method (28,29). We consequently chose several features for subsequent analyses: the "max contour position" is defined as the location of the

contour in the cell that has the highest intensity concentration, mapped to a number between 0 and 1, with 0 being the object center and 1 being the object perimeter. The maximal intensity pixel of DAPI was calculated using the "max pixel" feature (the largest value of DAPI pixel after background-subtraction). The "intensity of the side scatter" is the amount of light scattered 90° of the sample, illuminated by the 785 nm Laser. Cell areas were calculated using the "object mask" (segments images to closely identify the area corresponding to the cell) and the "area" feature (the number of microns squared in a mask, 1 pixel = 0.1089 μm^2) on bright-field images, and cell morphological changes were measured using the "circularity" feature (the average distance of the cell boundary from its center divided by the variation of this distance). For measuring VF fusion, "circularity" and "aspect ratio intensity" (the cell minor axis divided by the cell major axis of the best-fit ellipse, intensity weighted) were calculated from DAPI images based on 40% and 50% threshold masks, respectively. The area of high DAPI intensity was measured by the "area" feature, based on a threshold mask showing only the top 70% pixels in the DAPI channel of each cell. This cutoff was chosen as the highest threshold allowing only the VF area to be masked (Supporting Information Fig. S1).

Counting *Mimivirus* Virions Using IFC

Virus particles were collected from supernatants of infected cell cultures, concentrated by centrifugation, and stained for DNA (SYTO 59). Particle concentration was measured using IFC by counting (per volume) the positively stained particles with area and aspect ratio consistent with *Mimivirus* virions. We found the dynamic range of particle count to span over three orders of magnitude (Supporting Information Fig. S2).

Immunofluorescence Microscopy

A. polyphaga cells were cultured on glass microwell dishes (Mat-Tek corp. P35G-1.5-14-C) and infected with *Mimivirus* as described above. Cells were then blocked with 4% bovine serum albumin in PBS (BSA-PBS) for 30 min at RT and exposed for 2 h at RT to anti-tubulin antibody (DM1α; monoclonal anti-α-tubulin antibody; Sigma) diluted 1:400 in 4% BSA-PBS solution. Samples were then washed three times with PBS, followed by incubation with secondary antibody goat anti-mouse IgG conjugated to TRITC (Life Technologies, Carlsbad, CA) diluted 1:500 (for the Deltavision), or anti-mouse AlexaFluor 647 diluted 1:1500 (for the Vutara SRX200) in 4% BSA-PBS solution, DAPI (5 μg/ml) diluted 1:1000, and Phalloidin Alexa Fluor™ 488 (for the Deltavision) diluted 1:400 (Thermo Fisher Scientific, Waltham, MA) or Phalloidin Alexa Fluor® 568 (for the Vutara SRX200), all for 1 h at RT, and finally the samples were washed three times with PBS. Widefield fluorescence imaging was performed using a Deltavision microscope (Applied Precision, Rača, Slovakia) or Vutara SRX200 (Bruker, Billerica, MA) microscope. For the Deltavision system (equipped with 100X UPlanSApo NA 1.40 objective), images were acquired with a photometrics coolSNAP HQ2 CCD (Roper Scientific, Tucson, AZ) and deconvoluted with SoftWorx package using high noise filtering and 10 iterations. Image analysis and processing were conducted with Image J and Adobe Photoshop CS6-Extended software. Imaging with the Vutara SRX200 system was performed using a 60X NA 1.2 water immersion objective (Olympus, Waltham, MA) and Evolve 512 EMCCD camera (Photometrics, Huntington Beach, CA) with gain set of 50, and frame rate at 50 Hz.

Super-Resolution STORM Imaging

Super-resolution images were recorded with a Vutara SR 200 (Bruker) microscope based on the single-molecule localization biplane technology. Infected cells labeled with AlexaFluor 647 were imaged using a 647 nm excitation laser and a 405 nm activation laser. Imaging was done in a buffer composed of 5 mM cysteamine, oxygen scavengers (7 μl glucose oxidase and 56 nM catalase), 50 mM Tris, pH 8.0, with 10 mM NaCl and 10% glucose. Images were recorded using a 60X NA 1.2 water immersion objective (Olympus) and Evolve 512 EMCCD camera (Photometrics) with gain set at 50, frame rate at 50 Hz, and maximal power of 647 and 405 nm lasers set at 6 and 0.05 kW/cm^2, respectively. The total number of frames acquired was 5,000. Data were analyzed using the Vutara SRX software. Super-resolution images were overlaid with widefield DAPI images.

Statistical Analyses

In all graphs, error bars represent standard error calculated from biological replicates. Statistical analysis comparing different cell populations was conducted on each time point separately using ANOVA test, followed by Tukey post hoc test. Within each ANOVA model, the residuals were examined for normality, graphically and with a Shapiro-Wilks test. Deviations from normality were negligible and did not require data transformation. Figure 8A statistics were generated using Welch two Sample *t*-test (30). Statistical significance is marked with * when *P*-value <0.05, and ** when *P*-value <0.01.

Results

Selection of Optimal Features in IFC Data Reporting on *Mimivirus* Infection Stages

Parallel cultures of *A. polyphaga* cells were either left untreated or infected with *Mimivirus.* After 8 h, at which time infections were well-established, cultures were fixed and stained with DAPI. Fixation methods were optimized to preserve cell contours as described in the Materials and Methods section. Uninfected and 8-h timepoint samples (Supporting Information Fig. S3) were used to identify optimal IFC image features that distinguish infected from uninfected cells. The presence of a VF is a prominent trait of *Mimivirus*-infected cells and was used to identify successfully infected cells. Since the replication centers and VFs are the sites of viral DNA replication, they are clearly evident as intense, concentrated spots of DAPI staining, as previously reported from studies based on IF images of DAPI-stained *Mimivirus*-infected cells (4,10,11). Therefore, quantifying the area and the intensity of DAPI staining enabled us to determine the presence of a

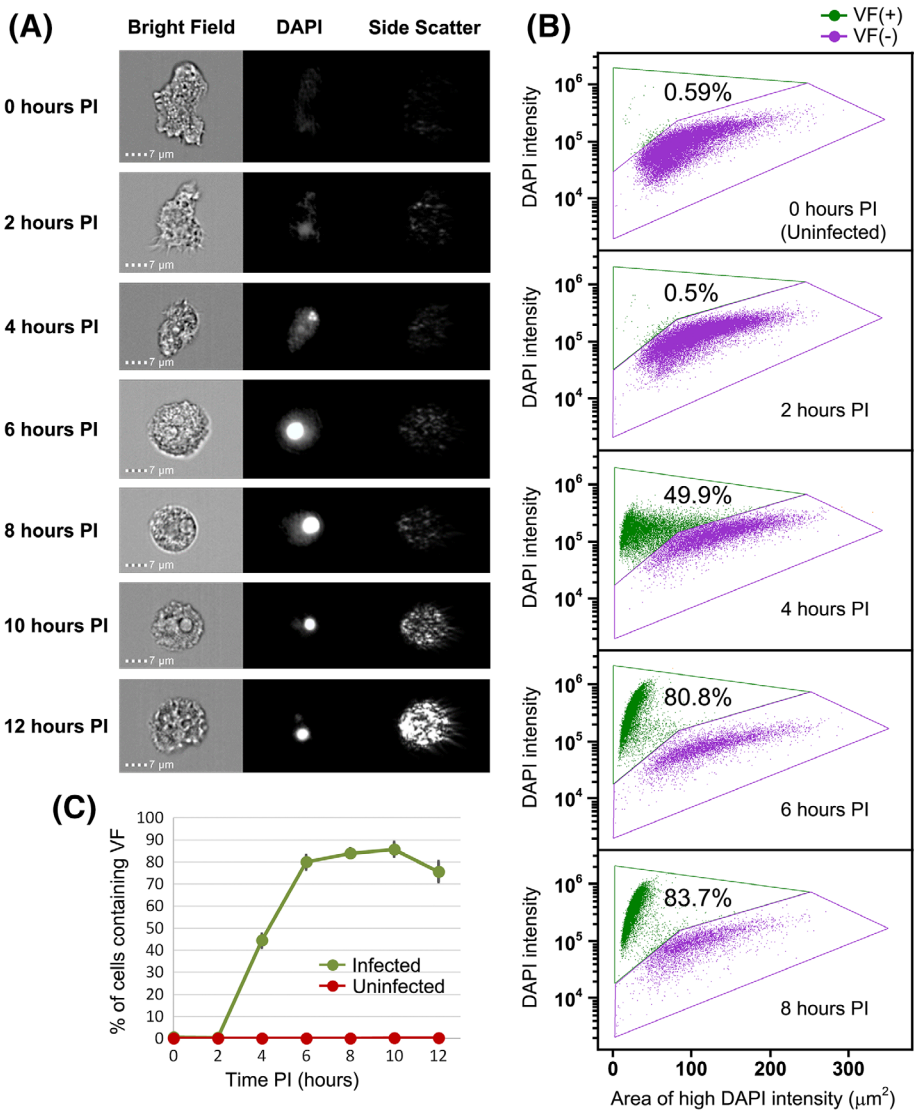

Figure 1. Detection of *Mimivirus* infected cell populations by IFC. The population of cells with viral factories was identified by measuring two parameters for each cell: The total intensity of DAPI staining and the area feature, based on a threshold mask showing only the top 70% pixels in the DAPI channel of each cell. Cells that contain a VF have significantly higher values of DAPI fluorescence, which is concentrated in a much smaller area of the cell. (**A**) Representative IFC pictures showing the bright field, DAPI, and SSC images of uninfected (0 h PI) and infected cells at different time points PI. (**B**) The distribution of cells that contain a VF (green gate) from the general population (purple gate) at 0, 2, 4, 6, and 8 h PI. The values in the green gate indicate the percent of cells in this population. (**C**) Percentage of cells containing a VF over time PI. Data are plotted as mean values, $N = 7$ at 0–8 h time points and $N = 4$ at 10 and 12 h time points. Error bars represent standard error.

replication center or a VF and define the infected population throughout the infection cycle.

After the IFC features distinguishing infected from uninfected cell populations were determined, data were recorded in three IFC channels: bright field to visualize cells contours, DAPI fluorescence to identify VFs, and side-scattered light (SSC) to detect newly formed virions (Fig. 1A). Though the nucleus and mitochondria of uninfected cells stained with DAPI, were detected by the IFC, staining of these organelles is poorly visible at the intensity display range suitable for VFs (Fig. 1A and Supporting Information Fig. S3). After data collection, various combinations of applied masks and features were examined and ranked by their RD values (Fisher's discriminant) (28,29). It was found that the features that differed most significantly between the infected and uninfected cell populations, and also corresponded to meaningful infection processes, were the following: intensity of DAPI fluorescence, area of high-intensity DAPI staining, the maximum pixel value of DAPI staining, localization of DAPI staining within the cell, cell circularity, and side scattering of light. The significance of each of these features to viral infection is described below.

Collection and Analysis of Kinetic Data on *Mimivirus* Infection

After establishing the features that distinguish *Mimivirus*-infected from uninfected cells, we performed a time-course of the infection, fixing cell samples at half-hour intervals postinfection (Fig. 1A and Supporting Information Fig. S4). From this experiment, it was determined that significant changes in the features characterizing infected cells can be recorded by collecting data at 2, 4, 6, 8, 10, and 12 h PI. Examining thousands of cells at each time point, we observed that about 80% of the cells became infected under the experimental conditions used (Fig. 1B).

For further analysis of viral infection kinetics, it was essential to focus on the infected cells by gating this population. We found that two features, namely DAPI intensity (total DAPI fluorescence intensity of each cell) and the area of high DAPI intensity (the number of pixels with DAPI fluorescence over a threshold mask showing only the top 70% pixels in the DAPI channel of each cell, see Methods and Supporting Information Fig. S1), separated the cells into two populations that were clearly distinct at 8 h PI (Fig. 1B). The gates of the populations were drawn based on their distribution at this time point and further verified by visual inspection of corresponding cells for VF presence. The gated region corresponding to infected cells began to be populated before 4 h PI and approached its maximum by 6 h PI (Fig. 1C). At early timepoints, most of the cells that did not fall within this gate were in fact infected, but as they did not yet show the features of viral replication centers, they could not be distinguished from uninfected cells on this basis. Therefore, data for the 0 and 2-h timepoints are presented for the entire population together; for 4 h PI and onwards, data are presented separately for cells within each gate.

We next measured the kinetics of key features by comparing the infected cell population (Fig. 2, VF(+) population, green lines) with the remaining population (Fig. 2, VF(−) population, purple lines). Feature values in the VF(−) population represent DAPI staining of the nucleus and mitochondria, whereas these values in the VF(+) population are dominated by DAPI staining of the VF. For all data presented, except for panel 2C, values for each feature were normalized to measurements on cells that had not been treated with *Mimivirus* (zero timepoint). Each of the features recorded using IFC reports on known processes in *Mimivirus* infection but provides for the first time quantification of the timing and amplitude of these processes across large populations.

Early events in viral infection center on DNA synthesis. The timing of VF production and maturation was followed using four features of the DAPI-channel images: total DAPI intensity, the area of high DAPI intensity, maximal intensity pixel of DAPI, and the cellular localization of DAPI-stained regions. These features represent DNA synthesis, the accumulation of the DNA in the VFs, DNA concentration within the VF, and the localization of the VFs relative to the cell center, respectively. The area of high DAPI intensity in the uninfected population (VF−) reflects the area of the nucleus plus the region of the cytoplasm containing mitochondria, which is heterogeneous due to cell mobility and cell cycle stage. In the infected population (VF+), area of high DAPI intensity reflects the size of replication centers, which remained compact throughout the infection (Fig. 2A). Notably, these sites are much brighter than the *A. polyphaga* nucleus, as reported previously (10,11), suggesting that they contain very high concentrations of DNA. Moreover, DAPI has high affinity toward A-T rich DNA (31) such as found in the *Mimivirus* genome (5). Though the area of high DAPI intensity remained relatively constant from 4 h PI onwards, the total DAPI intensity increased dramatically between 4 and 6 h PI and continued to increase until 8 h PI (Fig. 2B). This period represents a massive burst of viral DNA synthesis. During the same period, VFs translocated toward the cell center (Fig. 2C). The high concentration of DNA in the VF is further reflected by the maximum DAPI staining intensity, which reached 10 times the value measured at any site of an uninfected cell (Fig. 2D). At the late stage of the infection (8 h PI and on), both the total DAPI intensity and the maximum pixel intensity decreased by about 30% (Fig. 2B,D), consistent with a qualitative decrease in fluorescence reported previously (10). DNA replication rates may decrease at 8 h PI, due to virion assembly occur at this stage (Fig. 2E) and might reduce its staining with DAPI.

In addition to reporting on DNA production, IFC enabled quantification of two additional key processes: the accumulation of progeny virions inside the cell and morphological changes of the infected cells. These processes were reflected by the increase in the SSC intensity (Fig. 2E) and the circularity of the cells (Fig. 2F), respectively. SSC records the amount of light dispersed from particles inside the cell and as such measures the production of viral capsids and newly formed virions. Generation of VFs, in contrast, does not increase SSC, as the formation of VFs at 4 h PI (Fig. 2E, green line) and cellular events during the cell cycle of the host cell (Fig. 2E, purple line) do not increase SSC intensity. The accumulation of virions (4,8–11) and the rounding of infected cells (32–34) are established from previous studies using low-throughput microscopy methods. IFC showed that newly formed virions began to accumulate in the cell around 8 h PI and continued steadily until the end of the infection cycle, but changes in cell morphology occurred earlier, reaching the maximum at 8 h PI. Cells remained rounded until the end of the infection cycle.

Defining the kinetics of these major infection processes allowed us to reconstruct the *Mimivirus* infection cycle with high temporal resolution, resulting in a clear division into three main phases: 0–4 h PI, 4–6 h PI, and 6 h PI–cell lysis (Fig. 3).

Measuring Rates of Infection under Different Cell Perturbations

We next used our ability to determine viral infection kinetics on a population level from single-cell measurements to assess the effects of diverse cellular perturbations on the infection process. We first inspected the effect of generic oxidative stress (Fig. 4) by adding 500 μM H_2O_2 to the medium of infected cells at 30 min PI, and compared the kinetics of infection processes to those of parallel untreated infected cells. H_2O_2 treatment is cytotoxic and reduces the cell replication rate but does not lead to cell death, as cells recover their normal replication rate once the peroxide is washed out (unpublished data).

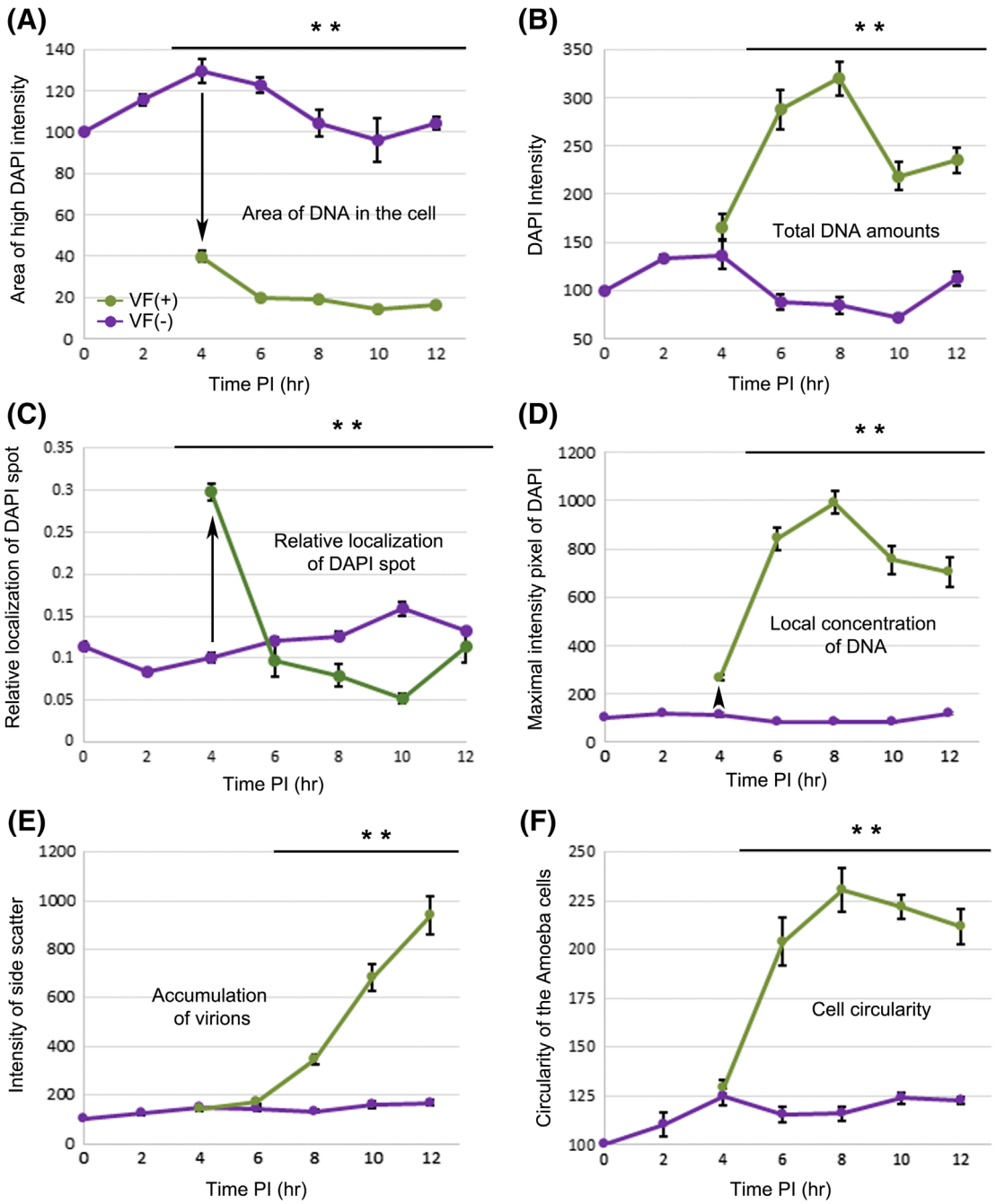

Figure 2. Tracking key processes throughout the infection cycle. Analyzing key features in the DAPI, bright field and SSC images of the VF-containing cell population (green line) compared with the rest of the cells (purple line), reveals great changes during the infection cycle. The values for each feature were normalized to the 0 h timepoints (uninfected cells) in all panels except C. (**A**) The area of high DAPI intensity (number of pixels with DAPI fluorescence over a threshold mask showing only the top 70% pixels in the DAPI image of each cell) was greatly reduced as the initial VFs were formed at 4 h PI, implying that most of the DNA in the VF-containing cells are located in these compartments. (**B**) The total amount of DNA in the cells was estimated by the DAPI intensity feature, which indicated that DNA replication started early in the infection and ended at 8 h PI. (**C**) The location of the VF relative to the cell center was calculated using the "Max Contour Position" feature, showing the DAPI spot transition from the cell periphery toward the center. (**D**) The accumulation of DNA in the VFs was measured using the "Max Pixel" feature, recording the highest pixel intensity of DAPI in a given cell, indicating the increasing local concentrations of DNA in the VFs as the infection progressed. (**E**) The intensity of SSC indicates a massive production of particles starting at 8 h PI and continuing until cells burst. (**F**) The degree of circularity reveals that most of the rounding up of the cells occurs between 4 and 8 h PI. Arrow indicates the appearance of the new VF-containing cell population at 4 h PI (green), out of the general population (purple). In all panels, data are plotted as mean values, $N = 7$ at 0–8 h time points and $N = 3$ at 10 and 12 h time points. Error bars represent standard error. At each timepoint, the VF(+) and VF(−) cell populations were compared and statistical significance calculated (* for $P < 0.05$, and **for $P < 0.01$).

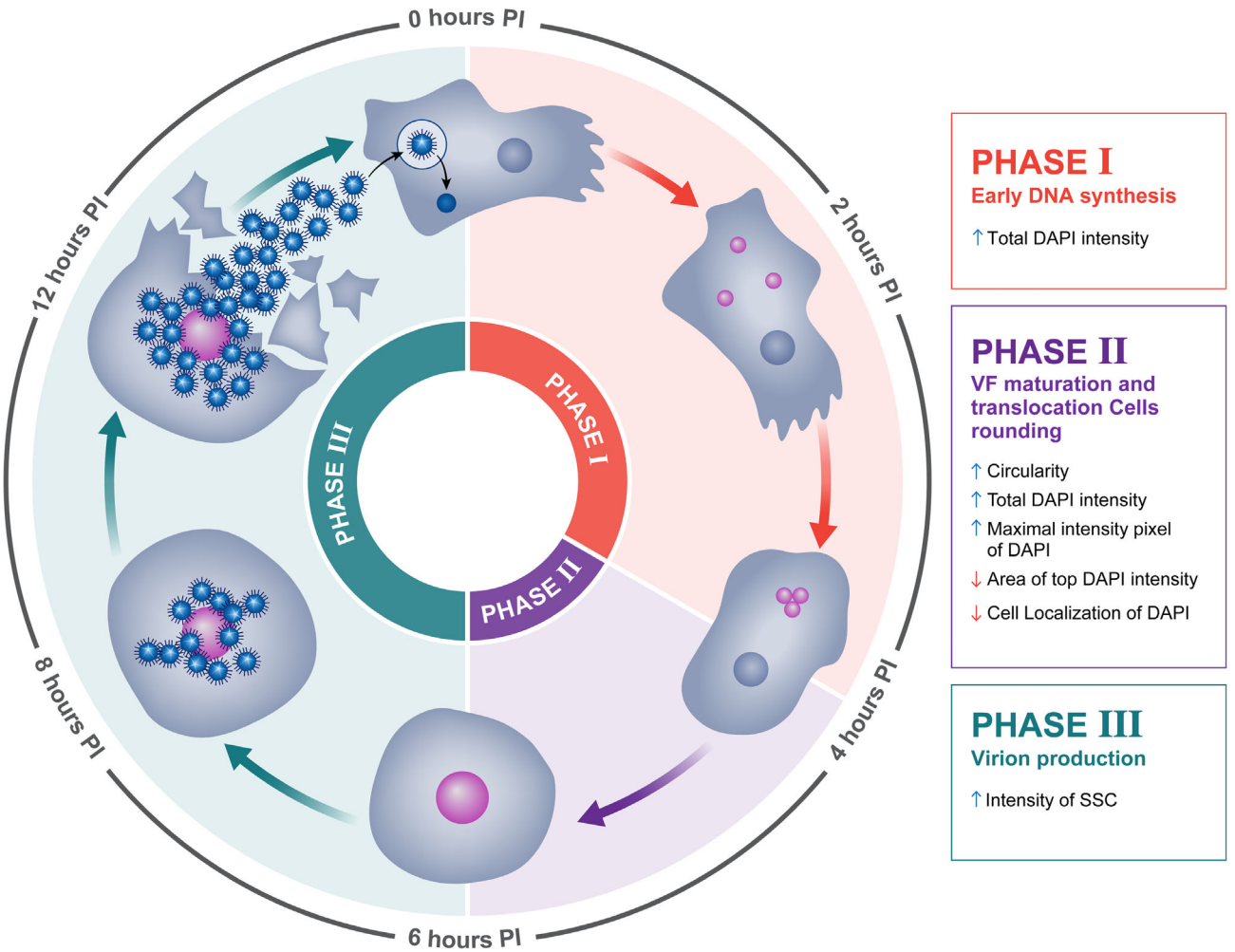

Figure 3. *Mimivirus* infection cycle scheme. According to our IFC results, the replication cycle can be divided into three main phases. Phase one: *Mimivirus* invades the host cell, viral genome is released into the host cell cytoplasm, and replication centers are generated within which viral DNA synthesis is initiated. Phase two: Initial replication centers coalesce and develop into mature VFs, the VFs are translocated toward the cell center, DNA is massively replicated and accumulates within the VFs, and the infected cells become smooth, spherical and immobile. Phase three: Capsids are produced, viral inner membranes are generated, viral genomes are assembled, and capsids are coated with fibrils as mature virions emerge.

Following H_2O_2 treatment, the generation of replication centers and VFs was significantly slower. Only at 12 h PI did replication center formation reach its peak, compared to 6 h for control, that is, infected but untreated samples (Fig. 4A). The fraction of H_2O_2-treated cells that eventually acquired a viral factory approached the fraction seen in control samples (about 80%). In accordance with the slower rate of replication center formation, DNA synthesis in the VFs was also delayed under the treatment. Only at 12 h PI did the DAPI intensity reach the peak value detected in the 8-h PI control samples (Fig. 4B). The translocation of the VF toward the cell center also appeared to be delayed, and although we detected some treated cells that developed VFs at 4 and 6 h PI, only at about 10 h PI were they found near the cell center (Fig. 4C).

Moreover, the H_2O_2 treatment appeared to delay the production of capsids and virions, as the SSC values of the treated samples began to increase only at 12 h PI, matching the levels of the control samples seen at 8 h PI (Fig. 4D). Both DNA accumulation and cell circularity were delayed but eventually reached the peak levels of the untreated cells at 10 or 12 h PI, respectively (Supporting Information Fig. S5A, B). For infection of H_2O_2-treated cells, the area of high DAPI in the VF-containing population decreased similarly to the control samples over the course of the infection, indicating that, although the VF generation rate was reduced, the VFs that were generated had a similar size (Supporting Information Fig. S5C).

To demonstrate that IFC can be used to construct accurate dose–response curves, we exposed infected cell cultures to increasing concentrations of H_2O_2 (100 to 1,000 μM) and measured the fraction of VF containing cells at 6 h PI (Fig. 4E). The fraction of cells containing a VF decreased as the concentration of H_2O_2 increased, and the IC_{50} for VF formation at 6 h PI, in this specific set of experiments, was

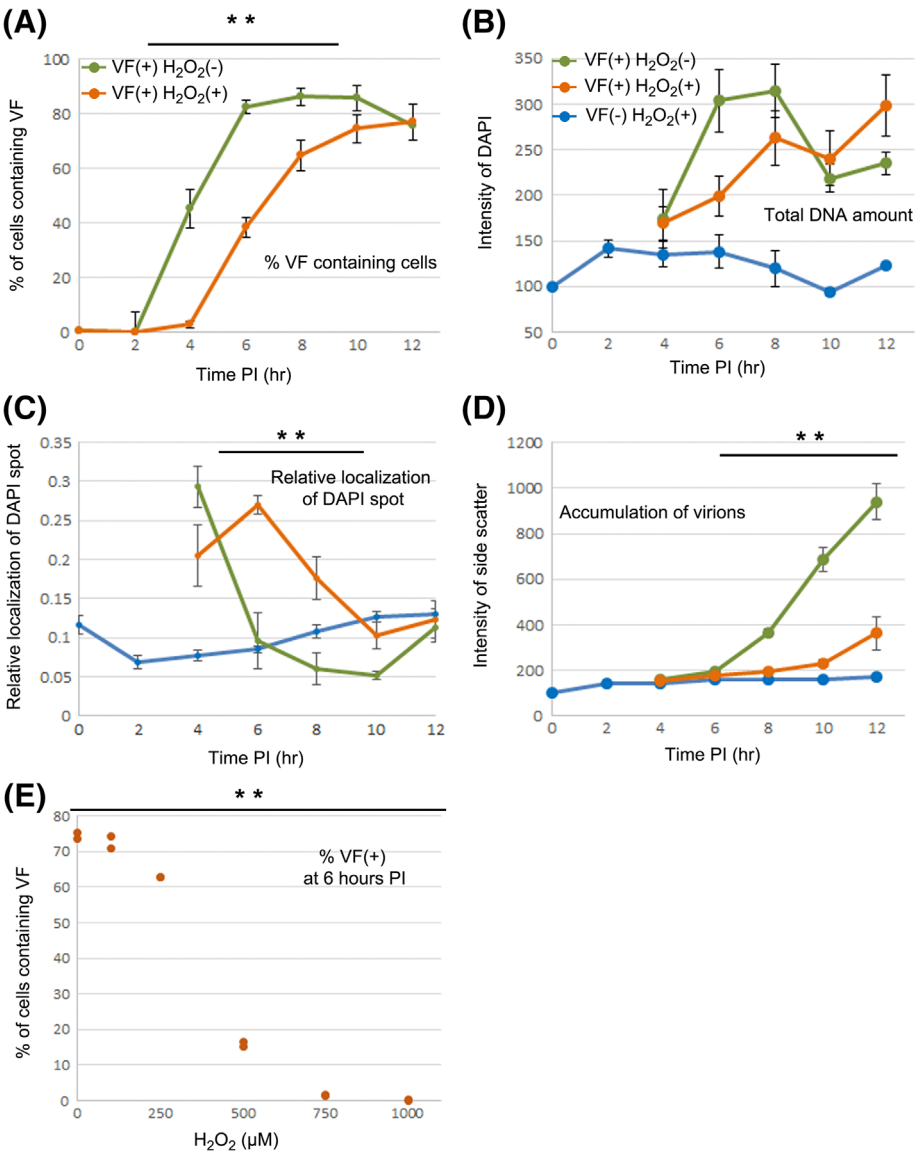

Figure 4. Tracking the delay in *Mimivirus* infection cycle progression under oxidative stress. (**A**) Percentage of cells containing VF over time PI, control infection compared with H_2O_2 treated samples. $N = 3$ at 0–8 h time points and N = 4 at 10 and 12 h time points. (**B–D**) Each graph presents the kinetics of the indicated feature of treated cells that contain no VF (blue), infected cells that contain VF (green), and infected and treated cells that contain VF (orange). (**E**) Percentage of cells containing VF at 6 h PI under treatments of H_2O_2 (100–1,000 μM). In all graphs, data are plotted as mean values, $N = 3$ (except in panel E, where $N = 2$), error bars represent standard error. At each timepoint, the VF(+) H_2O_2(–) and VF(+) H_2O_2(+) cell populations were compared and statistical significance calculated (** for $P < 0.01$).

calculated to be about 400 μM. The batch difference of *Mimivirus* and *A. polyphaga* cells is reflected here in their sensitivity to peroxide; in the first set of experiments about 40% of infected cells developed VFs at 6 h PI (Fig. 4A), whereas in a later batch only about 20% of the cells developed VFs (Fig. 4E) under the same H_2O_2 treatment (500 μM).

Mimivirus Infection Requires Certain Host Cytoskeleton Filaments

The cell cytoskeleton is known to participate in viral infection in vaccinia virus (35). As reported previously (32–34) and quantitated by our IFC analysis, cells infected with *Mimivirus* show a cytopathic effect, undergoing dramatic morphological changes likely to involve cytoskeleton rearrangements. To determine whether *Mimivirus* induces cell cytoskeleton alterations, we first monitored the structures of actin and tubulin fibers during infection. *Mimivirus*-infected cells were fixed at successive time points PI, actin or tubulin were fluorescently labeled, and filaments were imaged using super-resolution microscopy (Fig. 5). Microtubules in uninfected *A. polyphaga* cells consisted of long and curved filaments occupying almost the entire cytoplasm. About 4 h after the cells were infected, microtubules fragmented

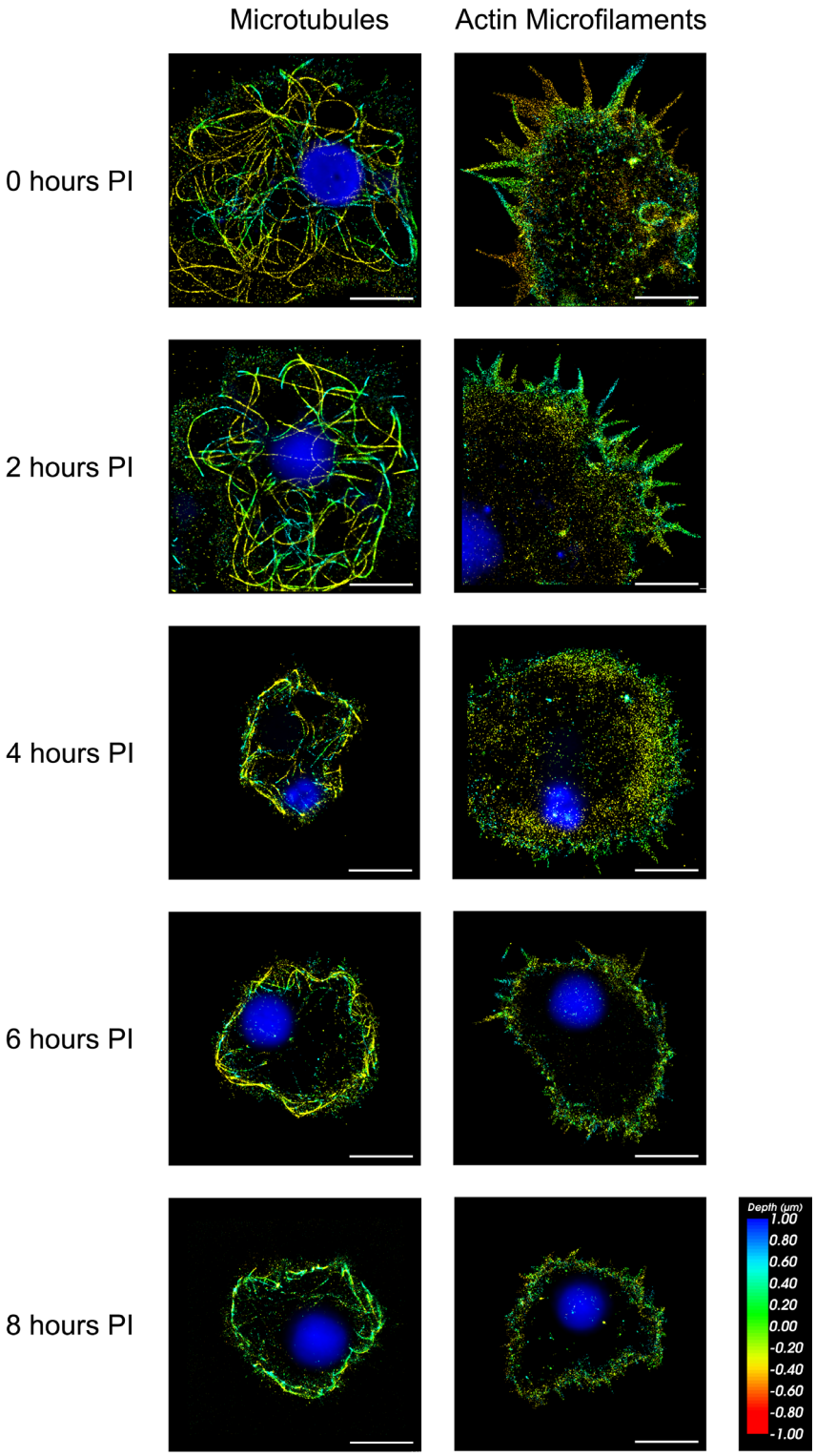

Figure 5. Cytoskeleton fibers structure throughout the infection cycle. Infected *A. polyphaga* cells were fixed at different time points PI, then microtubules (left column) or actin microfilaments (right column) were labeled with anti-α-tubulin or fluorescently labeled phalloidin, respectively, and cell nuclei (0–2 h PI) or the VF (4–8 h PI) were labeled with DNA stain (DAPI). The cells were then imaged using super-resolution microscopy (STORM) to reveal the structural changes of these fibers over time PI. X/Y scale bar equals 5 µm. The color code at the bottom right indicates depth in the *Z*-axis.

into shorter bundles, disappeared from the cell interior, and rearranged at the cell periphery as thick bundles (Fig. 5, left column). Actin microfilaments in uninfected cells in turn formed an elaborate array at the cell periphery, particularly in the pseudopodia and filopodia. When the cells were infected and began to round up, the actin microfilaments retracted from the pseudopodia and filopodia but remained at the cell periphery, forming a shell-like structure (Fig. 5, right column).

Disrupting *A. polyphaga* Cytoskeleton

To investigate the requirement for cytoskeleton in the infection cycle, we searched for effective reagents for disruption of cytoskeleton in *A. polyphaga*. Many cytoskeleton inhibitors are found to be ineffective on *Acanthamoeba* due to either decreased drug uptake, drug inactivation, or amino acid differences between cytoskeletal proteins of *A. polyphaga* and those of other organisms (36,37). Several tubulin and actin inhibitors were tested on *A. polyphaga* cells: phalloidin (250 μg/ml), paclitaxel (100 μM), and colchicine (16.6 mM) did not result in cell motility loss, cell detachment, or inhibition of cell proliferation, which are a few of the major outcomes expected of actin or microtubule inhibition (38,39). The microtubule disrupter vinblastine significantly inhibited cell proliferation but only at a high concentration of 1 mM, which might have been due to nonspecific interactions. We found the inhibitor of microtubule polymerization nocodazole (33 μM) and the inhibitor of actin polymerization latrunculin-B (5 μg/ml) to disrupt the respective filaments effectively, validated by fluorescence microscopy (Supporting Information Fig. S6) and by measuring significantly inhibited cell proliferation rates. Since the disrupted fibers were not structured, super-resolution microscopy did not provide additional information, and images were acquired by wide-field fluorescence microscopy. Both inhibitor doses were calibrated to achieve effective disruption of the respective filaments while keeping the cells alive, as cells recovered and continued to proliferate normally when these inhibitors were removed, even 8 h after treatment with nocodazole or latrunculin-B.

To obtain insight into the effects of cytoskeleton disruption on *Mimivirus* infection, *A. polyphaga* cells infected with *Mimivirus* were treated with nocodazole or latrunculin-B (or their vehicle controls—0.2% DMSO or 0.25% ethanol, respectively) and compared using IFC to control samples: infected and untreated cells, and uninfected and treated cells (Fig. 6). Surprisingly, we did not detect any significant effect on infection when we disrupted microtubules (Fig. 6 and Supporting Information Fig. S7, left columns). However, actin microfilament disruption severely affected the accumulation of new virions, as the intensity of the SSC at 8 h PI was ~60% lower than in control samples, while earlier processes were not significantly inhibited (Fig. 6 and Supporting Information Fig. S7, right columns).

Actin Disruption Inhibits Fusion of VFs

To study in more depth the effects of latrunculin-B on *Mimivirus* infection, we used fluorescence microscopy to examine cells at higher resolution. We found that the coalescence of multiple replication centers or VFs, normally observed shortly after their formation (4), was significantly hindered upon actin disruption (Fig. 7A and Supporting Information Fig. S8). To validate this result, we used IFC to image cells at 4, 6, and 8 h PI (Fig. 7B) and automatically counted the fraction of unfused VFs by using a combination of two features: circularity and aspect ratio, which applied together, can distinguish fused from unfused VFs. As the initial VFs fuse, the emerging mature VF is rounder and more condensed and therefore presents a higher aspect ratio (defined as the ratio of the minor to major axis of the VF) and a greater degree of circularity compared with unfused VFs (Fig. 7B,C). Thus, by gating cells presenting a VF with aspect ratio and circularity values below certain thresholds, we were able to calculate the fraction of cells containing unfused VFs (Supporting Information Fig. S9). Analyzing large populations of treated and control cells allowed us to validate and quantify the progression of VF fusion, and to measure the extent of its delay under actin disruption. We found that under normal conditions, VF fusion occurs mostly between 4 and 6 h PI (Fig. 7C, green bars), while under latrunculin-B treatment, at 6 and 8 h PI the treated samples had about 10 times more cells with unfused VFs compared with the control samples (Fig. 7C, orange lines).

Actin Disruption Reduces Viral Titers

Finally, we measured whether the disruption of microtubules or actin microfilaments affects the final release of infectious virions. We used an endpoint titration ($TCID_{50}$) assay, measuring the maximum dilution of the released virion suspension able to lyse *A. polyphaga* cells, to quantify the infectious particles released from nocodazole or latrunculin-B treated samples. We found no difference from the control samples in the viral titers of nocodazole-treated cells (Supporting Information Fig. S10). However, viral titers were reduced by 80% when cells were treated with latrunculin-B (Fig. 8A).

To further investigate whether this reduction of viral titers is a result of a decrease in the overall number of released virions, reduction in their infectious potential, or a combination of both, we stained the released particles with a DNA stain (SYTO 59) and used IFC to count *Mimivirus* particles (Materials and Methods, and Supporting Information Fig. S2). We found a decrease of 66% in the overall number of released particles at 22 h PI (Fig. 8B). Next, we infected *A. polyphaga* cells with equal numbers of virion particles released from untreated or treated samples, for a range of virion concentrations, and measured the fraction of VF-containing cells at 8 h PI. We found that the virions produced after latrunculin-B treatment were as infectious as control virions (Fig. 8C), indicating that the viral titer reduction measured by $TCID_{50}$ assay (Fig. 8A) is likely to reflect a decrease in the number of released virions (Fig. 8B) rather than a reduction in their infectious capacity.

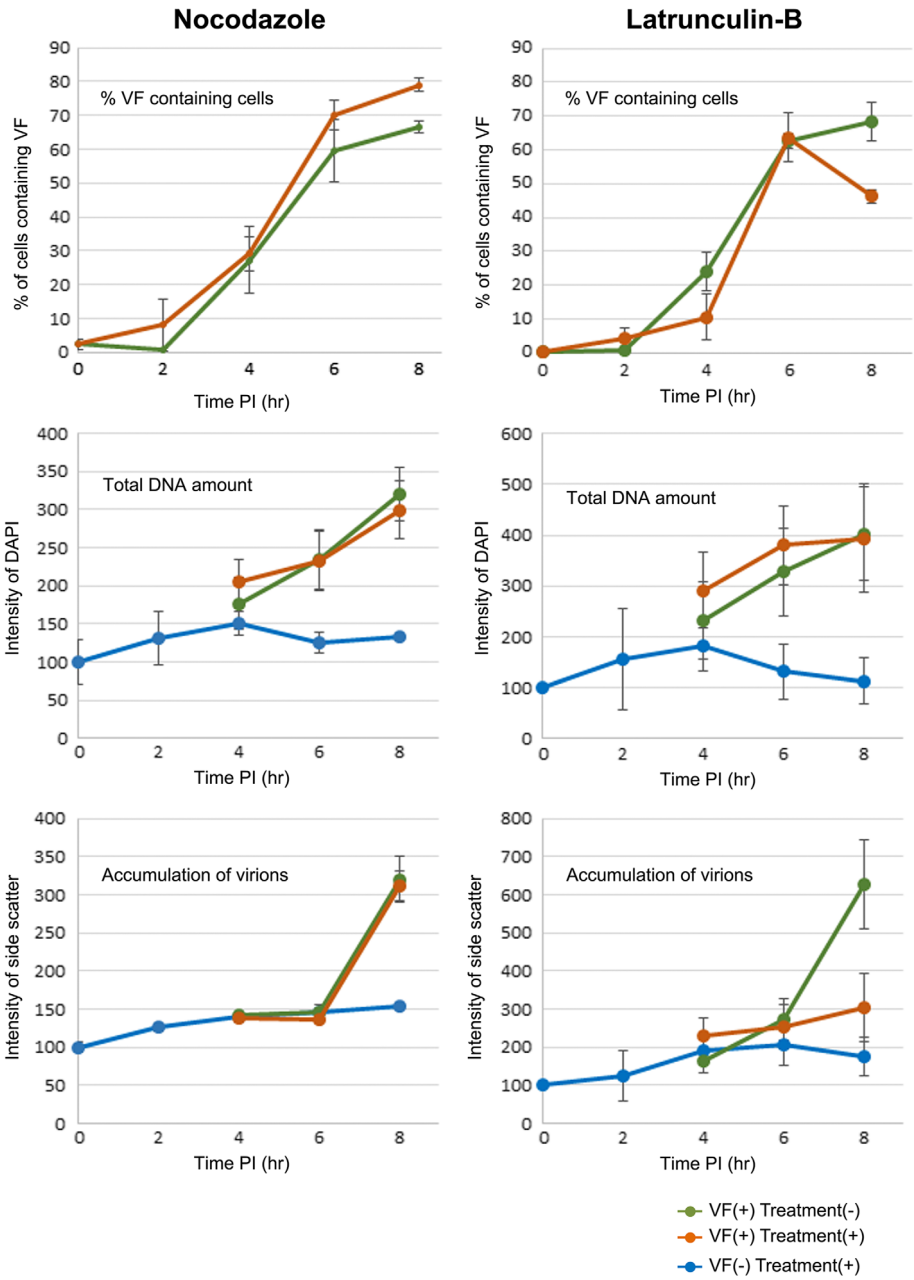

Figure 6. Tracking the delay in the progression of the infection cycle under the treatment of cytoskeleton inhibitors. Infected *A. polyphaga* cells treated with latrunculin-B (5 μg/ml) or nocodazole (33 μM) were fixed at different timepoints PI, stained with DAPI, and imaged using IFC. Treated and control cells were analyzed for the indicated features. Each graph presents the normalized values of the treated cells that contain no VF (blue), the untreated infected cells that contain a VF (green), and the treated cells that contain a VF (orange). Data are plotted as mean values, $N = 3$, error bars represent standard error.

Discussion

Since the discovery of the giant *Mimivirus*, most of the knowledge on its infection cycle has been obtained using advanced microscopy methods, which provide highly detailed structural data but are limited in their small field of view, allowing just a few cells to be imaged at a time. We wished to complement these methodologies by analyzing images of large populations of infected cells at key time points PI, to reveal accurate time windows and kinetics of major infection processes. Aligning these processes along a time line, and in accordance with observations reported previously (4,8–11), we could assemble them into three major temporal phases: 0–4 h PI, 4–6 h PI, and 6 h PI to cell lysis (Fig. 3). This division was achieved independently, but it is consistent with a previous division of the *Mimivirus* replication cycle into three temporal and functional stages based on gene expression profiles (40).

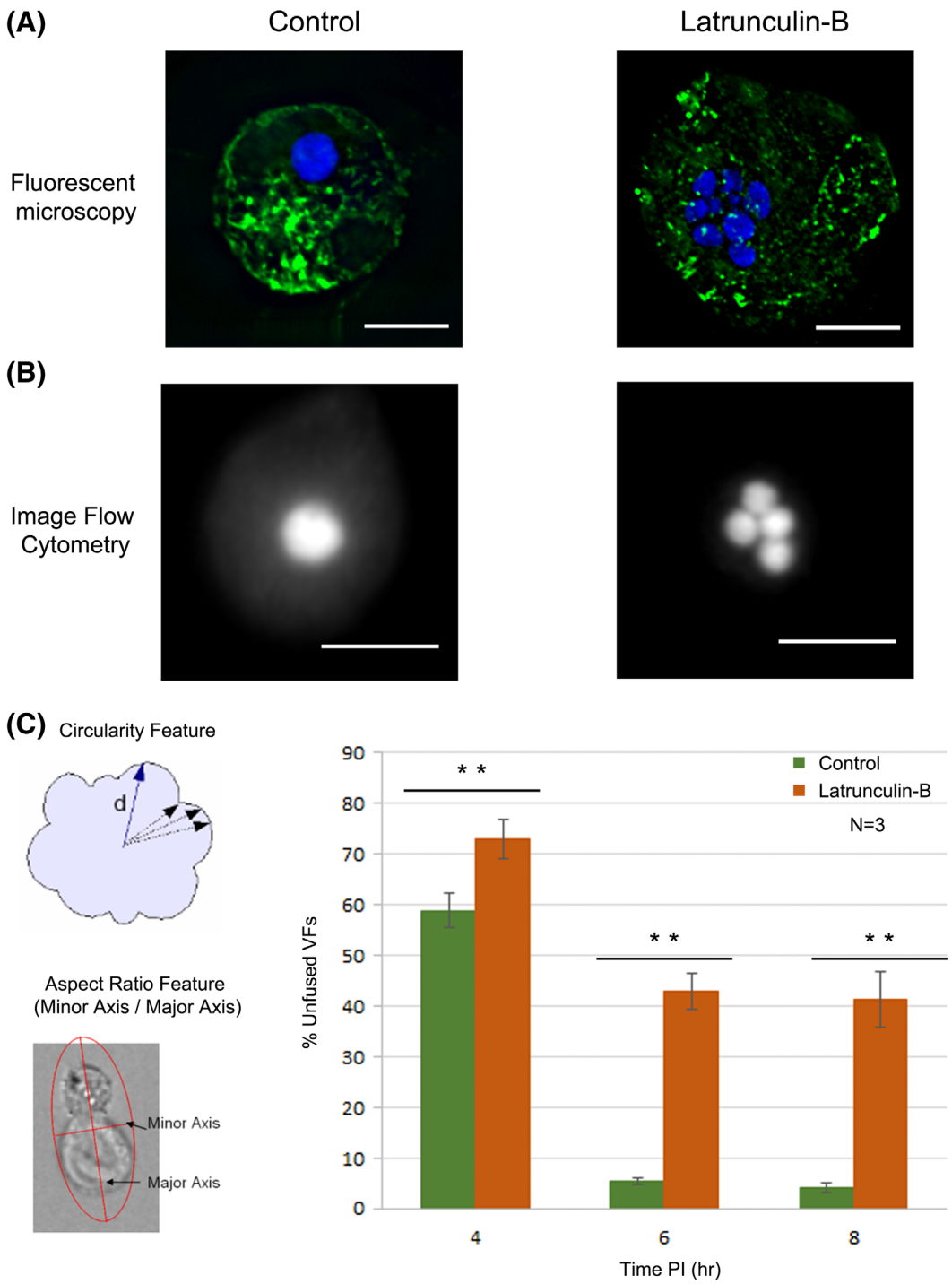

Figure 7. Measuring the inhibition of VF fusion under latrunculin-B treatment. Infected *A. polyphaga* cells were treated with latrunculin-B (5 μg/ml) or ethanol as control (0.25%), fixed at 8 h PI, and VFs were recorded by (**A**) fluorescence microscopy (DNA stain—DAPI in blue, actin microfilaments stain—fluorescent phalloidin in green), scale bar = 10 μm. (**B**) IFC imaging (DAPI channel), scale bar = 10 μm. (**C**) Infected cells were treated with latrunculin-B and fixed at 4, 6, and 8 h PI, then stained with DAPI and imaged by IFC. The sample images were analyzed for having fused or unfused VF using two features: VF circularity and VF aspect ratio (the VF minor axis divided by its major axis, as illustrated). Cells containing VFs that have low circularity and aspect ratio were gated as unfused, and their fraction of the total VF containing population is presented in the graph. $N = 3$, error bars represent standard error. Statistical significance is marked as ** for $P < 0.01$.

During the first phase, from 0 to 4 h PI, the virus invades the host, releases its genome into the host cell cytoplasm, and replication centers (apparently one per infecting virus) are generated, within which viral DNA synthesis is initiated. The second phase, occurring between 4 and 6 h PI, consists of significant changes preparing the infected cells for

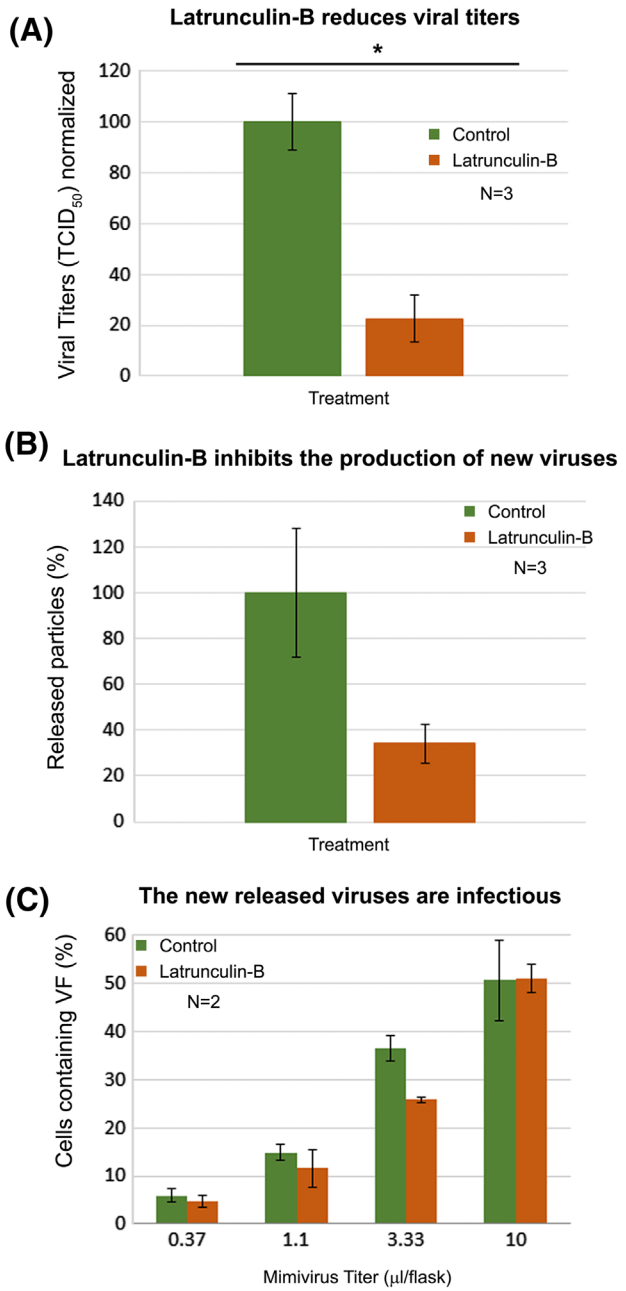

Figure 8. Measuring reduced viral yields under latrunculin-B treatment. (**A**) Infected *A. polyphaga* cells were treated with latrunculin-B (5 μg/ml) or ethanol as control (0.25%), and the number of infectious virions released at the end of the infection was measured using endpoint titration ($TCID_{50}$) assay. The treated cells presented a reduction of 80% in the number of released particles. $N = 3$. (**B**) The concentration of released particles from control or treated samples was measured by IFC, to reveal a 66% reduction in the number of released particles at 20 h PI under latrunculin-B treatment. (**C**) *A. polyphaga* cells were infected with increasing titers of *Mimivirus* released from the latrunculin-B treated or control samples, and the infection potential was measured by the fraction of cells presenting VF at 8 h PI. $N = 2$. Error bars represent standard error in all plots. Statistical significance is marked as * for $P < 0.05$.

the subsequent assembly of virions. During this phase, initial replication centers coalesce and evolve into mature VFs (Fig. 7C). Along with the development of VFs, they translocate toward the cell center (Fig. 2C), and DNA massively accumulates within them. Significantly, our measurements imply that DNA concentration in mature VFs is 10 times higher than in nuclei of uninfected *A. polyphaga* cells (Fig. 2D). Within the same timeframe, the infected cells change their typical trophozoite spread morphology, lose surface features (i.e., pseudopods) and become smooth, spherical, and immobile. As all these processes take place simultaneously, the second phase appears as the most prominent in the infection cycle. During the final phase, occurring between 6 h PI and cell lysis, capsids are produced, viral inner membranes are generated (11), viral genomes are assembled, and capsids are coated with fibrils as mature virions emerge (8). This build-up and assembly of virions proceed until the final burst of cells and release of virion progeny occur. Notably, our IFC results are consistent with previous observations derived from structural studies and bioinformatics (41–43) but, as discussed below, they provide novel quantitative aspects of the infection cycle.

The IFC data reveal a clear temporal separation between processes occurring during the second and third infection phases. Specifically, formation and assembly of viral progeny in the third phase seem to begin only upon completion of DNA synthesis in the second phase. This sharp transition suggests that completion of DNA synthesis triggers formation and assembly of virions in a manner analogous to cell cycle checkpoints. Notably, under oxidative stress, infected cells show a delay of about 2 h in DNA synthesis. Virion formation, as monitored by SSC, is also delayed to the same extent. Several scenarios can be envisioned for the coupling of capsid production to the end of DNA synthesis. The most straightforward is that transcription of late genes, including the capsid, is done mostly from newly synthesized DNA, and as more DNA becomes available, transcription rate increases. Alternatively, reaching a threshold level of DNA or depletion of raw materials may trigger a signal that initiates capsid production, as genes encoding structural components of the *Mimivirus* particle are found under a "late" promoter element and are mainly transcribed at this temporal phase (40).

Utilizing IFC to inspect specific aspects of *Mimivirus*–cell interactions, we analyzed whether and how cytoskeletal changes contribute to the infection. We suspected that the cell cytoskeleton must rearrange, for two main reasons. First, cells undergo substantial morphological transformations during infection. Second, other viruses, and specifically vaccinia virus (VV), which is a member of the NCLDV clade, use their host cytoskeleton during replication. VV, herpesvirus, and murine leukemia virus were reported to interact with microtubules or with their motor proteins, kinesins and dyneins, to cross the dense cytosol toward the nucleus, or to translocate toward the plasma membrane to exit the cell without lysis (44–52). In addition, VV and herpes viruses were shown to modify the cortical actin framework, which serves as a barrier for egress, as they interact with

actin and myosin to facilitate their direct spread between cells (53–56). Furthermore, the intermediate filament vimentin was found to rearrange to form a cage-like structure around the VF of African swine fever virus (another member of the NCLDV clade) during infection, but the causes and purposes of this rearrangement are unknown (57). However, it has also been observed that disruption of the host cytoskeleton did not affect replication or virion yields for some of these viruses (58,59).

Using super-resolution microscopy, we monitored microtubules and actin microfilaments, (currently, there is no evidence for intermediate filaments in *Acanthamoeba*), and found both to undergo major structural transformations as the cells round up and become immobile during the second infection phase at 4–6 h PI. We suggest that the translocation of microtubules to the cell periphery may clear space for the VF to mature and expand in the cell center as well as allow for massive production of virions. Notably, such a microtubule rearrangement may be an outcome of changes in the actin network due to viral infection, and thus microtubules may not be direct or active participants in *Mimivirus* infection. Supporting this idea, microtubules rearrange to produce a similar pattern as that detected at 4 h PI and on, just shortly after actin microfilament disruption is induced by latrunculin B (Supporting Information Fig. S6C, left column). Moreover, microtubule disruption with nocodazole early during infection had no effect on the infection processes or on the number of released infectious particles (Supporting Information Fig. S10). For comparison, microtubules are required for VV replication sites to collect in the perinuclear area, for actin rearrangements during VV replication, and for intracellular transport and distribution of virions. Although (as for *Mimivirus*) nocodazole treatment does not significantly affect VV virion production, the above processes are inhibited or completely blocked upon treatment, implying that microtubules are required for VV replication (60–64).

To investigate whether actin microfilaments are required for *Mimivirus* infection, we disrupted these filaments using latrunculin-B and observed defects in the fusion of replication centers into a mature VF and the production of new virions (Figs. 7 and 8). Likewise, disrupting actin microfilaments in VV infected cells decreased the number of released virus particles (56,65,66). This may imply a similar, yet to be identified, use of host actin microfilaments by these two NCLDV viruses. Further studies on how *Mimivirus* utilizes the *Acanthamoeba* cytoskeleton may shed light on additional fundamental issues of the viral infection cycle. For example, does the virus use the actin cytoskeleton for translocating itself, the VF, or the newly formed virions through the dense cytosol?

Finally, we propose that the IFC platform can be utilized to study the infection cycles of other viruses, especially other recently discovered VF-forming giant viruses, to examine and quantify viral–host interactions, and to explore the progress of infection under different perturbations. Image-based cell sorting techniques currently being developed (67,68) could be used to further study subpopulations of resistant cells or to correlate infection rates with cellular features in search for specific viral–host interactions.

Literature Cited

1. Dixon LK, Chapman DAG, Netherton CL, Upton C. African swine fever virus replication and genomics. Virus Res 2013;173:3–14.
2. Milrot E, Mutsafi Y, Fridmann-Sirkis Y, Shimoni E, Rechav K, Gurnon JR, Van Etten JL, Minsky A. Virus-host interactions: Insights from the replication cycle of the large *Paramecium bursaria* chlorella virus. Cell Microbiol 2016;18:3–16.
3. Moss B. Poxvirus DNA replication. Cold Spring Harb Perspect Biol 2013;5:a010199.
4. Mutsafi Y, Zauberman N, Sabanay I, Minsky A. Vaccinia-like cytoplasmic replication of the giant mimivirus. Proc Natl Acad Sci USA 2010;107:5978–5982.
5. Raoult D, Audic S, Robert C, Abergel C, Renesto P, Ogata H, La Scola B, Suzan M, Claverie JM. The 1.2-megabase genome sequence of Mimivirus. Science (80-) 2004; 306:1344–1350.
6. Renesto P, Abergel C, Decloquement P, Moinier D, Azza S, Ogata H, Fourquet P, Gorvel J-P, Claverie J-M. Mimivirus giant particles incorporate a large fraction of anonymous and unique gene products. J Virol 2006;80:11678–11685.
7. Fridmann-Sirkis Y, Milrot E, Mutsafi Y, Ben-Dor S, Levin Y, Savidor A, Kartvelishvily E, Minsky A. Efficiency in complexity: Composition and dynamic nature of mimivirus replication factories. J Virol 2016;90:10039–10047.
8. Zauberman N, Mutsafi Y, Halevy DB, Shimoni E, Klein E, Xiao C, Sun S, Minsky A. Distinct DNA exit and packaging portals in the virus *Acanthamoeba polyphaga* mimivirus. PLoS Biol 2008;6:1104–1114.
9. Andrade ACDSP, Rodrigues RAL, Oliveira GP, Andrade KR, Bonjardim CA, La Scola B, Kroon EG, Abrahão JS. Filling knowledge gaps for mimivirus entry, uncoating, and morphogenesis. J Virol 2017;91:e01335-17.
10. Suzan-Monti M, La Scola B, Barrassi L, Espinosa L, Raoult D. Ultrastructural characterization of the giant volcano-like virus factory of *Acanthamoeba polyphaga* mimivirus. PLoS One 2007;2:e328.
11. Mutsafi Y, Shimoni E, Shimon A, Minsky A. Membrane assembly during the infection cycle of the giant mimivirus. PLoS Pathog 2013;9:e1003367.
12. Arslan D, Legendre M, Seltzer V, Abergel C, Claverie J-M. Distant mimivirus relative with a larger genome highlights the fundamental features of megaviridae. Proc Natl Acad Sci USA 2011;108:17486–17491.
13. Legendre M, Santini S, Rico A, Abergel C, Claverie JM. Breaking the 1000-gene barrier for mimivirus using ultra-deep genome and transcriptome sequencing. Virol J 2011;8:99.
14. Moreira D, Brochier-Armanet C. Giant viruses, giant chimeras: The multiple evolutionary histories of mimivirus genes. BMC Evol Biol 2008;8:12.
15. Villarreal LP, Witzany G. Viruses are essential agents within the roots and stem of the tree of life. J Theor Biol 2010;262:698–710.
16. Legendre M, Arslan D, Abergel C, Claverie J-M. Genomics of megavirus and the elusive fourth domain of life. Commun Integr Biol 2012;5:102–106.
17. Xiao C, Chipman PR, Battisti AJ, Bowman VD, Renesto P, Raoult D, Rossmann MG. Cryo-electron microscopy of the giant mimivirus. J Mol Biol 2005; 353:493–496.
18. Xiao C, Kuznetsov YG, Sun S, Hafenstein SL, Kostyuchenko VA, Chipman PR, Suzan-Monti M, Raoult D, McPherson A, Rossmann MG. Structural studies of the giant mimivirus. PLoS Biol 2009;7:e92.
19. Ekeberg T, Svenda M, Abergel C, Maia FRNC, Seltzer V, Claverie J-M, Hantke M, Jönsson O, Nettelblad C, van der Schot G, et al. Three-dimensional reconstruction of the giant mimivirus particle with an X-ray free-electron laser. Phys Rev Lett 2015;114:098102.
20. Ekeberg T, Svenda M, Seibert MM, Abergel C, Maia FRNC, Seltzer V, DePonte DP, Aquila A, Andreasson J, Iwan B, et al. Single-shot diffraction data from the Mimivirus particle using an X-ray free-electron laser. Sci Data 2016;3:160060.
21. Kuznetsov YG, Xiao C, Sun S, Raoult D, Rossmann M, McPherson A. Atomic force microscopy investigation of the giant mimivirus. Virology 2010;404:127–137.
22. Gibson-Corley KN, Bockenstedt MM, Li H, Boggiatto PM, Phanse Y, Petersen CA, Bellaire BH, Jones DE. An in vitro model of antibody-enhanced killing of the intracellular parasite leishmania amazonensis. PLoS One 2014;9:1–8.
23. Lagal V, Dinis M, Cannella D, Bargieri D, Gonzalez V, Andenmatten N, Meissner M, Tardieux I. AMA1-deficient *Toxoplasma gondii* parasites transiently colonize mice and trigger an innate immune response that leads to long-lasting protective immunity. Infect Immun 2015;83:2475–2486.
24. Yason JA, Tan KSW. Seeing the whole elephant: Imaging flow cytometry reveals extensive morphological diversity within blastocystis isolates. PLoS One 2015;10:1–15.
25. Johansson J, Karlsson A, Bylund J, Welin A. Phagocyte interactions with *Mycobacterium tuberculosis*—Simultaneous analysis of phagocytosis, phagosome maturation and intracellular replication by imaging flow cytometry. J Immunol Methods 2015;427:73–84.
26. Dekel E, Rivkin A, Heidenreich M, Nadav Y, Ofir-Birin Y, Porat Z, Regev-Rudzki N. Identification and classification of the malaria parasite blood developmental stages, using imaging flow cytometry. Methods 2017;112:157–166.
27. George TC, Fanning SL, Fitzgerald-Bocarsly P, Fitzgeral-Bocarsly P, Medeiros RB, Highfill S, Shimizu Y, Hall BE, Frost K, Basiji D, et al. Quantitative measurement of nuclear translocation events using similarity analysis of multispectral cellular images obtained in flow. J Immunol Methods 2006;311:117–129.
28. Marangon I, Boggetto N, Ménard-Moyon C, Luciani N, Wilhelm C, Bianco A, Gazeau F. Localization and relative quantification of carbon nanotubes in cells with multispectral imaging flow cytometry. J Vis Exp 2013;82:e50566.
29. Wortzel I, Koifman G, Rotter V, Seger R, Porat Z. High throughput analysis of Golgi structure by imaging flow cytometry. Sci Rep 2017;7:788.
30. Zar JH. Biostatistical analysis. 5th ed. Upper Saddle River, NJ: Prentice-Hall/-Pearson, 2010.
31. Williamson DH, Fennell DJ. Chapter 16: The use of fluorescent DNA-binding agent for detecting and separating yeast mitochondrial DNA. In: Prescott DM, editor.

Methods in Cell Biology. Volume 12. New York, NY: Academic Press, 1975; p. 335–351.

32. Monier A, Larsen JB, Sandaa RA, Bratbak G, Claverie JM, Ogata H. Marine mimivirus relatives are probably large algal viruses. Virol J 2008;5:1–8.
33. Abrahão J, Silva L, Silva LS, Khalil JYB, Rodrigues R, Arantes T, Assis F, Boratto P, Andrade M, Kroon EG, et al. Tailed giant Tupanvirus possesses the most complete translational apparatus of the known virosphere. Nat Commun 2018;9:749.
34. Abrahão JS, Boratto P, Dornas FP, Silva LC, Campos RK, Almeida GMF, Kroon EG, La Scola B. Growing a giant: Evaluation of the virological parameters for mimivirus production. J Virol Methods 2014;207:6–11.
35. Leite F, Way M. The role of signalling and the cytoskeleton during Vaccinia virus egress. Virus Res 2015;209:87–99.
36. Khan NA. Acanthamoeba: Biology and Pathogenesis. 2nd ed. Norfolk, UK: Caister Academic Press, 2015.
37. Henriquez FL, Ingram PR, Muench SP, Rice DW, Roberts CW. Molecular basis for resistance of acanthamoeba tubulins to all major classes of antitubulin compounds. Antimicrob Agents Chemother 2008;52:1133–1135.
38. Joos L, Gicquaud C. Effect of phalloidin and viroisin on *Acanthamoeba castellanii* after permeabilization of the cell. Biochem Cell Biol 1987;65:261–270.
39. Peterson JR, Mitchison TJ. Small molecules, big impact: A history of chemical inhibitors and the cytoskeleton. Chem Biol 2002;9:1275–1285.
40. Legendre M, Audic S, Poirot O, Hingamp P, Seltzer V, Byrne D, Lartigue A, Lescot M, Bernadac A, Poulain J, et al. mRNA deep sequencing reveals 75 new genes and a complex transcriptional landscape in mimivirus. Genome Res 2010;20:664–674.
41. Boratto PVM, Dornas FP, Andrade KR, Rodrigues R, Peixoto F, Silva LCF, La Scola B, Costa AO, de Almeida GMF, Kroon EG, et al. Amoebas as mimivirus bunkers: Increased resistance to UV light, heat and chemical biocides when viruses are carried by amoeba hosts. Arch Virol 2014;159:1039–1043.
42. Marciano-Cabral F, Cabral G. Acanthamoeba spp. as agents of disease in humans. Clin Microbiol Rev 2003;16:273–307.
43. Kraemer JA, Erb ML, Waddling CA, Montabana EA, Zehr EA, Wang H, Nguyen K, Pham DSL, Agard DA, Pogliano J. A phage tubulin assembles dynamic filaments by an atypical mechanism to center viral DNA within the host cell. Cell 2012;149: 1488–1499.
44. Schepis A, Stauber T, Krijnse Locker J. Kinesin-1 plays multiple roles during the vaccinia virus life cycle. Cell Microbiol 2007;9:1960–1973.
45. Sanderson CM, Hollinshead M, Smith GL. The vaccinia virus A27L protein is needed for the microtubule-dependent transport of intracellular mature virus particles. J Gen Virol 2000;81:47–58.
46. Carter GC, Rodger G, Murphy BJ, Law M, Krauss O, Hollinshead M, Smith GL. Vaccinia virus cores are transported on microtubules. J Gen Virol 2003;84: 2443–2458.
47. Mallardo M, Schleich S, Krijnse Locker J. Microtubule-dependent organization of vaccinia virus core-derived early mRNAs into distinct cytoplasmic structures. Mol Biol Cell 2001;12:3875–3891.
48. Arakawa Y, Cordeiro JV, Way M. F11L-mediated inhibition of RhoA-mDia signaling stimulates microtubule dynamics during vaccinia virus infection. Cell Host Microbe 2007;1:213–226.
49. Diefenbach RJ, Miranda-Saksena M, Diefenbach E, Holland DJ, Boadle RA, Armati PJ, Cunningham AL. Herpes simplex virus tegument protein US11 interacts with conventional kinesin heavy chain. J Virol 2002;76:3282–3291.
50. Lee GE, Murray JW, Wolkoff AW, Wilson DW. Reconstitution of herpes simplex virus microtubule-dependent trafficking in vitro. J Virol 2006;80:4264–4275.
51. Koshizuka T, Kawaguchi Y, Nishiyama Y. Herpes simplex virus type 2 membrane protein UL56 associates with the kinesin motor protein KIF1A. J Gen Virol 2005;86: 527–533.
52. Kim W, Tang Y, Okada Y, Torrey TA, Chattopadhyay SK, Pfleiderer M, Falkner FG, Dorner F, Choi W, Hirokawa N, et al. Binding of murine leukemia virus gag polyproteins to KIF4, a microtubule-based motor protein. J Virol 1998;72: 6898–6901.
53. Cudmore S, Cossart P, Griffiths G, Way M. Actin-based motility of vaccinia virus. Nature 1995;378:636–638.
54. Roberts KL, Baines JD. Myosin Va enhances secretion of herpes simplex virus 1 virions and cell surface expression of viral glycoproteins. J Virol 2010;84: 9889–9896.
55. Cordeiro JV, Guerra S, Arakawa Y, Dodding MP, Esteban M, Way M. F11-mediated inhibition of RhoA signalling enhances the spread of vaccinia virus in vitro and in vivo in an intranasal mouse model of infection. PLoS One 2009;4:e8506.
56. Arakawa Y, Cordeiro JV, Schleich S, Newsome TP, Way M. The release of vaccinia virus from infected cells requires RhoA-mDia modulation of cortical actin. Cell Host Microbe 2007;1:227–240.
57. Stefanovic S, Windsor M, Nagata K-I, Inagaki M, Wileman T. Vimentin rearrangement during African swine fever virus infection involves retrograde transport along microtubules and phosphorylation of vimentin by calcium calmodulin kinase II. J Virol 2005;79:11766–11775.
58. Matthews JD, Morgan R, Sleigher C, Frey TK. Do viruses require the cytoskeleton? Virol J 2013;10:121.
59. Matthews JD, Tzeng W-P, Frey TK. Analysis of the function of cytoplasmic fibers formed by the rubella virus nonstructural replicase proteins. Virology 2010;406: 212–227.
60. Ploubidou A, Moreau V, Ashman K, Reckmann I, González C, Way M. Vaccinia virus infection disrupts microtubule organization and centrosome function. EMBO J 2000;19:3932–3944.
61. Ward BM, Moss B. Vaccinia virus intracellular movement is associated with microtubules and independent of actin tails. J Virol 2001;75:11651–11663.
62. Hollinshead M, Rodger G, Van Eijl H, Law M, Hollinshead R, Vaux DJ, Smith GL. Vaccinia virus utilizes microtubules for movement to the cell surface. J Cell Biol 2001;154:389–402.
63. Schepis A, Schramm B, de Haan CAM, Locker JK. Vaccinia virus-induced microtubule-dependent cellular rearrangements. Traffic 2006;7:308–323.
64. Schramm B, de Haan CAM, Young J, Doglio L, Schleich S, Reese C, Popov AV, Steffen W, Schroer T, Locker JK. Vaccinia-virus-induced cellular contractility facilitates the subcellular localization of the viral replication sites. Traffic 2006;7: 1352–1367.
65. Huang C-Y, Lu T-Y, Bair C-H, Chang Y-S, Jwo J-K, Chang W. A novel cellular protein, VPEF, facilitates vaccinia virus penetration into HeLa cells through fluid phase endocytosis. J Virol 2008;82:7988–7999.
66. Sandgren KJ, Wilkinson J, Miranda-Saksena M, McInerney GM, Byth-Wilson K, Robinson PJ, Cunningham AL. A differential role for macropinocytosis in mediating entry of the two forms of vaccinia virus into dendritic cells. PLoS Pathog 2010;6: e1000866.
67. Nitta N, Sugimura T, Isozaki A, Mikami H, Hiraki K, Sakuma S, Iino T, Arai F, Endo T, Fujiwaki Y, et al. Intelligent image-activated cell sorting. Cell 2018;175: 266–276.e13.
68. Brasko C, Smith K, Molnar C, Farago N, Hegedus L, Balind A, Balassa T, Szkalisity A, Sukosd F, Kocsis K, et al. Intelligent image-based in situ single-cell isolation. Nat Commun 2018;9:226.